Xueyuan Nie*

Numerical analysis of geometrical nonlinear aeroelasticity with CFD/CSD method

https://doi.org/10.1515/ijnsns-2015-0096
Received July 13, 2015; accepted February 22, 2021; published online March 17, 2021

Abstract: A nonlinear static aeroelastic methodology based on the coupled CFD/CSD approach has been developed to study the geometrical nonlinear aeroelastic behaviors of high-aspect-ratio or multi-material flexible aerial vehicles under aerodynamic loads. The Reynolds-averaged Navier–Stokes solver combined with the three-dimensional finite-element nonlinear solver is used to perform the fluid-structure coupling simulation. The interpolation technique for data transfer between the aerodynamic and structural modules employs radial basis function algorithm as well as dynamic mesh deformation. A high-aspect-ratio structure with multi-material is modeled by the finite element method to investigate the effects of geometrical nonlinearity on the aeroelastic behavior. Numerical simulations of the linear and nonlinear static aeroelasticity were conducted at transonic regime with different angles of attack. By comparing the aeroelastic behaviors of linear and nonlinear structure, it shows that geometrical nonlinearity plays an important role for flexible high-aspect-ratio wings undergoing the large static aeroelastic deformation and should be taken into account in aeroelastic analysis for such structures.

Keywords: aeroelasticity; geometric nonlinearity; nonlinear aerodynamics; nonlinear finite element method.

1 Introduction

With the growing advances of demands for aerospace industry, much attention has been given to develop aircrafts which can fly more higher, farther and faster. The high-aspect-ratio lifting surfaces to achieve the desired high lift-to-drag ratio and composite material to obtain the minimum structural weight designs are commonly used in high-altitude long-endurance vehicles and wide-body aircrafts to satisfy all performance and schedule constraints. From the structural viewpoint, this leads to very flexible constructions. Such aircrafts often undergo large deflections, which sometimes give rise to adverse or even disastrous effects on the structure and induce the structural geometrical nonlinearity.

Fluid–structure interaction has played an important role in aeroelastic stability analysis. In the recent 20 years, many numerical simulations have been adopted to study aeroelastic behavior with geometrical nonlinearity. As a whole, they can be roughly categorized into two types of approaches according to involved aerodynamic loads computation method. One is linear aerodynamic theory with beam model. Patil et al. [1–3] investigated geometrical nonlinearity effects on the static and dynamic aeroelastic behavior, with stall model ONERA [4] which originates from trip theory or doublet-lattice theory, combined with geometrically exact beam model, and demonstrated the change in structural frequencies and aeroelastic response due to geometrical nonlinearity. Another is nonlinear aerodynamic equation with nonlinear beam model. Patil et al. used Euler solver coupled geometrically exact beam to study aeroelastic behavior of a high-aspect-ratio wing and concluded that linear aerodynamic models may cause overly conservative predictions in divergence and flutter speed. Garcia and Guruswamy [5] used Navier–Stokes solutions for fully nonlinear aeroelastic analysis

***Corresponding author: Xueyuan Nie**, Key Laboratory for Mechanics in Fluid Solid Coupling Systems, Institute of Mechanics, Chinese Academy of Sciences, Beijing 100190, China, E-mail: niexueyuan@imech.ac.cn

of slender wings modeled by nonlinear beam element. Previous literatures, which study on the geometrical nonlinear aeroelasticity, mainly focus on the aircrafts in subsonic regime.

1-D beam models can reflect the average deformations of the practical 3-D wings. However, they cannot provide the actual elastic solution in 3-D domain [6]. Linear aerodynamics model is limited to inviscid flows which do not have strong shocks or vortical flow regions associated with them. When performing aeroelastic analysis of complex configuration or accurately predicting geometrically nonlinear aeroelastic behavior, high fidelity methods based on Navier–Stokes equations coupled with 3-D structural finite element model should be used.

In this article, the aeroelastic behavior of a wide-body airplane with a real composite wing is investigated with Reynolds-average Navier–Stokes solver and 3-D elastic structure dynamics solver in transonic regime. This article is divided into four sections. First, a brief introduction of fluid–structure interaction key components including the fluid dynamics solver, nonlinear structural solver, moving grid deformation scheme and data interpolation approach are given. Then the composite material finite element structural model and CFD model used in here are described. In the third section, the linear and nonlinear static aeroelastic responses are simulated, and the differences between them are compared and discussed. Finally, some concluding remarks are offered.

2 CFD/CSD coupling methodology

Fluid–structure interaction procedure in this article is loosely coupled algorithm, in which unsteady Navier–Stokes equations with radial basis function (RBF) mesh deformation technique are solved to obtain the unsteady information about flow fields, and nonlinear structural solver is adopted to account for the geometrical nonlinearity caused by large deformation. In addition, there exists the transfer of information between CFD and CSD: surface loads from the aerodynamics to the structure, and surface displacement from the structure to the aerodynamics. RBF method is also employed for the transfer. In both solvers, the internal sub-iterations are usually necessary to achieve convergence of their nonlinear equations.

2.1 Unsteady Navier–Stokes solver

Unsteady aerodynamics computations are performed by three-dimensional RANs Navier–Stokes control equations and have been coded by the Institute of Mechanics, Chinese Academy of Sciences (CAS). The integral form of the conservation equation on an arbitrary control volume V with moving boundary can be written as [7],

$$\frac{\partial}{\partial t}\int_V \mathbf{Q}\,\mathrm{d}V + \oint_S (\mathbf{G}_\mathrm{c} - \mathbf{G}_\mathrm{v})\,\mathbf{n}\,\mathrm{d}S = 0 \tag{1}$$

where $\mathbf{Q}$ is conserved quantity vector, $\mathbf{G}_\mathrm{c}$ and $\mathbf{G}_\mathrm{v}$ represent convective and viscous flux vectors, respectively, S denotes the boundary of the control volume V, S is the face area scalar and $\boldsymbol{n}$ denotes the face normal vector. Equation (1) is spatially discretized by finite volume method as,

$$\frac{\mathrm{d}}{\mathrm{d}t}\mathbf{Q}_I V_I = -\sum_{m=1}^{N_\mathrm{F}} (\mathbf{G}_\mathrm{c} - \mathbf{G}_\mathrm{v})_m\,\Delta\mathbf{S}_m \tag{2}$$

where V_I is the volume of the Ith grid cell, N_F is the number of faces around the Ith cell, $\Delta\mathbf{S}_m$ is the normal area of the mth surface. Two-equation turbulence k–w model is used to derive the closed Navier–Stokes equations.

For suppressing numerical oscillations and capturing the shock, Roe difference scheme [8] with high shock resolution is used to discretize the convective terms and can be written by,

$$(\mathbf{F}_\mathrm{c})_{I+1/2} = \frac{1}{2}\left(\mathbf{F}_\mathrm{c}^\mathrm{R} + \mathbf{F}_\mathrm{c}^\mathrm{L}\right) - \frac{1}{2}|\mathbf{A}|_{I+1/2}\,(\mathbf{Q}_\mathrm{R} - \mathbf{Q}_\mathrm{L}) \tag{3}$$

where $\boldsymbol{A}$ is Roe matrix. Viscous terms are discretized by second-order center difference scheme. Dual time stepping implicit format is used to temporal discretization of Eq. (2), and Eq. (4) can be obtained as

$$\frac{3V_I^{n+1}\mathbf{Q}_I^{n+1} - 4V_I^n\mathbf{Q}_I^n + V_I^{n-1}\mathbf{Q}_I^{n-1}}{2\Delta t} = -\mathbf{R}_I^{n+1}(\mathbf{Q}_I^{n+1}) \tag{4}$$

where $\mathbf{R}_\mathrm{I}$ generally called residual represents the right-hand side of Eq. (2). In present computation, pseudo time is introduced to eliminate time-marching error. After some deduction, Eq. (4) can then be finally written as follows,

$$\left(\left(\frac{1}{\tau^*} + \frac{3}{2\Delta t}\right)V_I^{(n+1)} + \frac{\partial \mathbf{R}_I}{\partial \mathbf{Q}_I}\right)\Delta\mathbf{Q}_I^{*(m)} = -\frac{3V^{(n+1)}\mathbf{Q}_I^{*(m)} - 4V^{(n)}\mathbf{Q}_I^{(n)} + V^{(n-1)}\mathbf{Q}_I^{(n-1)}}{2\Delta t} - \mathbf{R}_I^{*(m)} \tag{5}$$

where asterisk denotes pseudo quantities and m is pseudo time step. Lower-upper Symmetric Gauss-Seidel algorithm is adopted to achieve implicit solutions.

The above CFD solver has been parallelized with Message Passing Interface (MPI) and has good resolution in space and time and computation efficiency. It can predict the flows from subsonic to hypersonic flow regimes and has been used in many engineering applications (Yang, 2011, 2014) [9] to validate the algorithm effectiveness and efficiency.

2.2 Nonlinear structural solver

Linear analysis assumes a linear relationship between the load applied to a structure and the response of the structure. The stiffness of a structure in a linear analysis does not change depending on its previous state. Linear static problems are solved in one step, by a single decomposition of the stiffness matrix. For a very flexible structure here, the large deflections cannot meet the infinitesimal deformation restrictions, and the stiffness of the structures changes and must be accounted for by regenerating the stiffness matrix. In the study, such change roots in large deformations, that is to say, geometric nonlinearity. MSC Nastran has an excellent ability to analyze structural problems subjected to geometric nonlinearities (MSC.software) [10].

Nonlinear problems require incremental solution schemes that divide the problem into steps calculating the displacement, and then updating the stiffness. Each step uses the results from the previous step as a starting point. As a result, the stiffness matrix must be generated and decomposed many times during the analysis. We adopt the total Lagrangian approach based on the initial element geometry by using the LGDISP parameter. This method is suitable for problems where moderately large rotations but small strains occur. The equilibrium equation can be expressed by the principle of virtual work as,

$$\int_{V_0} {}^{t+\Delta t}_{0}S_{ij}\,\delta\,{}^{t+\Delta t}_{0}E_{ij}\,\mathrm{d}V = \int_{V_0} b_i^0\,\delta\eta_i\,\mathrm{d}V + \int_{A_0} t_i^0\,\delta\eta_i\,\mathrm{d}A \tag{6}$$

Here V_0 is the volume of the initial configuration, ${}^{t+\Delta t}_{0}S_{ij}$ is the symmetric second Piola–Kirchhoff stress tensor, ${}^{t+\Delta t}_{0}E_{ij}$ is the Green–Lagrange strain, b_i^0 is the body force in the reference configuration, t_i^0 is the traction vector in the reference configuration and η_i is the virtual displacements. Integrations are carried out in the original configuration at $t = 0$. Introduce incremental decomposition for the stress tensor and the strains as following,

$${}^{t+\Delta t}_{0}S_{ij} = {}^{t}_{0}S_{ij} + \Delta S_{ij} \tag{7.1}$$

$${}^{t+\Delta t}_{0}E_{ij} = {}^{t}_{0}E_{ij} + \Delta E_{ij} \tag{7.2}$$

where ${}^{t}_{0}S_{ij}$ and ${}^{t}_{0}E_{ij}$ are the total stress and strains for equilibrated configurations, respectively, ΔS_{ij} and ΔE_{ij} are the incremental stress and strains between t and $t + \Delta t$. The incremental strains are further decomposed into linear $\Delta E_{ij}^{\mathrm{l}}$ and nonlinear $\Delta E_{ij}^{\mathrm{nl}}$ parts as,

$$\Delta E_{ij} = \Delta E_{ij}^{\mathrm{l}} + \Delta E_{ij}^{\mathrm{nl}} \tag{8}$$

where $\Delta E_{ij}^{\mathrm{l}} = \frac{1}{2}\left(\Delta u_{i,j} + \Delta u_{j,i} + {}_0^t u_{k,i}\Delta u_{k,j} + {}_0^t u_{k,j}\Delta u_{k,i}\right)$, $\Delta E_{ij}^{\mathrm{nl}} = \frac{1}{2}\left(\Delta u_{k,i}\Delta u_{k,j}\right)$.

Linearization of equilibrium of Eq. (6) yields,

$$\left({}_0^t\mathbf{K}_{\mathrm{L}} + {}_0^t\mathbf{K}_{\mathrm{NL}}\right)\Delta\mathbf{u} = {}^{t+\Delta t}\mathbf{Q} - {}^t\mathbf{F} \tag{9}$$

where ${}_0^t K_{\mathrm{L}}$ is linear stiffness matrix, ${}_0^t K_{\mathrm{NL}}$ is called nonlinear stiffness composed of initial displacement stiffness matrix and initial stress stiffness matrix [11], $\Delta\mathbf{u}$ is incremental displacement vector, ${}^{t+\Delta t}\mathbf{Q}$ and ${}^t\mathbf{F}$ are the external and internal forces, respectively.

Newton–Raphson iterative algorithm is employed to solve the equilibrium problem described in Eq. (9) at each load increment. The total load is applied gradually in steps (or increments) and for each load step, the solution is arrived at after one or more iterations. Each iteration involves an assembly and solution of the stiffness matrix. Hence, nonlinear problems inherently take longer than linear models (of the same size) to solve. At the end of each iteration, a check is made to see if the solution has converged. If the convergence check fails, the iteration is re-repeated with the new information; and it is re-assembled and re-solved. This process repeats until convergence is achieved. Following that, the next increment of load is applied. The load increments are applied until the full load of the model is solved. Here, for static problems, $t + \Delta t$ stands for load increment not for time.

2.3 Mesh deformation and data transfer technique

Aerodynamic analysis requires a higher degree of mesh resolution than structural analysis, and the mismatch between structure grids and the fluid grids demands interdisciplinary transfer of data involving aerodynamic loads converted to structural loads and structural deformations presented on the aerodynamic surface. In the study, the RBF method [12] is used to accomplish the above two-way data exchange and grid deformation. The essence of the method is described below. Interpolants are constructed based on scattered points with given displacements located at the deforming component. These displacements are then propagated into the interior of the mesh by evaluating the interpolants at all mesh points.

The formulation of the RBF interpolation model used in the study is

$$s(\mathbf{r}) = \sum_{i=1}^{N_{\mathrm{s}}} \gamma_i \varphi\left(\left\|\mathbf{r} - r_i\right\|\right) + p(\mathbf{r}) \tag{10}$$

where s is the function to be evaluated at point $\mathbf{r}$, φ is the RBF adopted which have several forms as described by Beckert and Wendland [13], N_{s} is the numbers of the centers for RBFs and r_i is the center point location. The coefficients γ_i are found by requiring exact recovery of the original function; in this study the structural displacement $p(\mathbf{r})$ is the optional polynomial. In two-way data transfer, let $p(\mathbf{r}) = a_0 + a_1 x + a_2 y + a_3 z$ to satisfy conservations of force and moment. In mesh deformation, $p(\mathbf{r})$ is not used.

The interpolation problem is described in the following matrix expression as

$$\mathbf{u}_{sx} = \mathbf{C}_{ss}\mathbf{a}_x \tag{11}$$

where $\mathbf{U}_{sx} = (\mathbf{u}_{sx} 0\ 0\ 0\ 0)^T$ is displacement vector in x-direction,

$$a_x = \left(\gamma_1, \ \ldots, \ \gamma_{N_{\mathrm{s}}}\ a_0\ \ a_1\ \ a_2\ \ a_3\ \right)^T \tag{12}$$

$$\mathbf{C}_{ss} = \begin{bmatrix} \varphi\left(\|\mathbf{r}_1 - \mathbf{r}_1\|\right) & \cdots & \varphi\left(\left\|\mathbf{r}_1 - \mathbf{r}_{N_s}\right\|\right) & 1 & x_1 & y_1 & z_1 \\ \vdots & \vdots & \vdots & \vdots & \vdots & \vdots & \vdots \\ \varphi\left(\left\|\mathbf{r}_{N_s} - \mathbf{r}_1\right\|\right) & \cdots & \varphi\left(\left\|\mathbf{r}_{N_s} - \mathbf{r}_{N_s}\right\|\right) & 1 & x_{N_s} & y_{N_s} & z_{N_s} \\ 1 & \cdots & 1 & 0 & 0 & 0 & 0 \\ x_1 & y_1 & z_1 & 0 & 0 & 0 & 0 \\ \vdots & \vdots & \vdots & \vdots & \vdots & \vdots & \vdots \\ x_{N_s} & y_{N_s} & z_{N_s} & 0 & 0 & 0 & 0 \end{bmatrix} \tag{13}$$

If used in mesh deform, the later four rows in the above three terms are removed. Here, RBF function formulation is selected as

$$\varphi\left(\|\mathbf{r} - \mathbf{r}_i\|\right) = \left(1 - \frac{\|\mathbf{r} - \mathbf{r}_i\|}{R}\right)^4 \left(4\frac{\|\mathbf{r} - \mathbf{r}_i\|}{R} + 1\right) \tag{14}$$

R is support radius to control the region of influence of the center.

By solving Eq. (11), the coefficients matrix expressed by Eq. (12) can be obtained. An analogous matrix $\mathbf{C}_{as}$ is created to interpolate displacements of aerodynamic surface from structure displacements.

$$\mathbf{C}_{as} = \begin{bmatrix} \varphi\left(\|\mathbf{r}_1 - \mathbf{r}_1\|\right) & \cdots & \varphi\left(\left\|\mathbf{r}_1 - \mathbf{r}_{N_s}\right\|\right) & 1 & x_1 & y_1 & z_1 \\ \vdots & \vdots & \vdots & \vdots & \vdots & \vdots & \vdots \\ \varphi\left(\left\|\mathbf{r}_{N_a} - \mathbf{r}_1\right\|\right) & \cdots & \varphi\left(\left\|\mathbf{r}_{N_a} - \mathbf{r}_{N_s}\right\|\right) & 1 & x_{N_a} & y_{N_a} & z_{N_a} \end{bmatrix} \tag{15}$$

$$\mathbf{u}_{ax} = \mathbf{C}_{as}\mathbf{a}_x \tag{16}$$

where N_a is the number of aerodynamic surface nodes and $\mathbf{u}_{ax}$ is the corresponding displacement vector.

On the above basis, with greedy sampling strategy [14], some of the aerodynamic surface nodes are selected to interpolate the mesh grid deformation. The procedure resembles the interpolation between structure displacement and aerodynamic displacement. The only difference is that the last four rows in Eq. (13) need to be removed when used in the mesh grid deformation. In addition, in terms of the enormous number of the volume mesh nodes, the computation of mesh deformation is realized by MPI parallelization.

The procedure described in the section can be depicted as below (Figure 1).

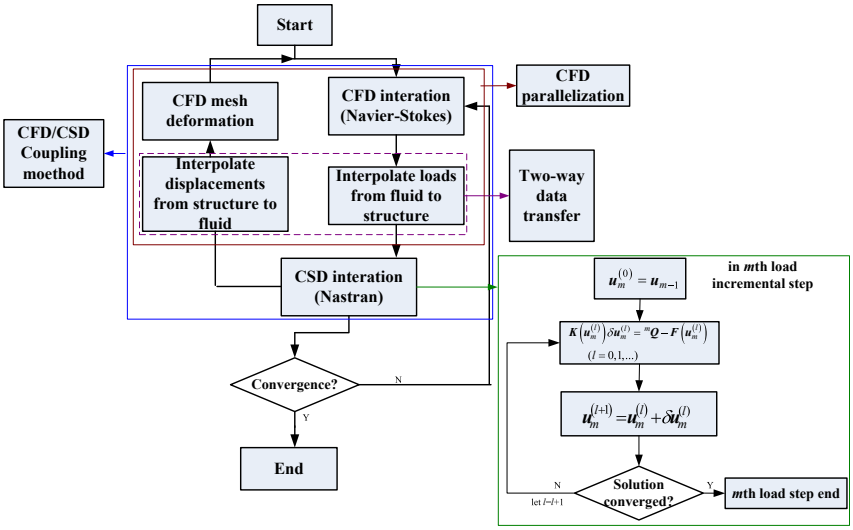

Figure 1: CFD/CSD coupling procedure.

3 Numerical example

A multi-composite material wing with the engine pylon used for wide-body aircraft is selected to investigate structural geometrical nonlinearity effects on aeroelastic behavior. The wing has an aspect ratio of 9.4, a taper ratio of 0.4 and a quarter chord swept angle of 32°. The airfoil thickness is 14% at root and 10% at tip. The chord root length is 11,634 mm. Material fiber directions are designed to make the wing suffer geometrical bending-torsion coupling effect while chordwise bending or flapwise bending occurs.

3.1 Structural model

The wing structure consists of wing boxes and wing ribs, whose finite element model has been developed using 4-node, 3-node shell elements and 2-node beam elements. For the engine pylon finite element model is modeled by beam elements, concentrated mass elements and rigid bar elements. All composite laminates comprise 0, ±45 and 90° plies. The thickness of all the plies are constrained to be equal. The number of elements is 6019 and the number of discrete DOF is 5760. The structural model of the wing used in the research is shown in Figure 2.

3.2 Aerodynamic model

The structured multi-block mesh has been generated for CFD computation in the example. The semi-symmetrical model is used as the aerodynamic model. O-type grid topology is used to enclose the fuselage surface with the height of approximate 400 mm to create the boundary layer region. The first cell height is 1×10^{-5} of the wing root chord length with a growth rate of 1.2. H-type grid topology is adopted to create volume mesh except the boundary layer. The outer domain is about 6–7 times the root chord length. The whole volume domain has about 17.35 million cells as shown in Figure 3(a), where the blue lines represent the boundaries of the multi-block mesh. The zoomed mesh of the surface and symmetrical plane is shown in Figure 3(b).

3.3 Results and discussion

Nonlinear static aeroelastic results are computed at the same Mach number of 0.85 and at different angles of attack of 0°, 2.46°, 4° and 8°, where 2.46° is the trimming angle of attack. Figure 4 shows the convergence of the residuals and largest displacement over the wing surface for nonlinear static aeroelastic case with the free-stream Mach number of 0.85 and the angle of attack 8°. Residuals represent L2 norm of the density residual, $\Delta U_{\max}$ represents the maximum displacement (at the wing tip in this case) in vertical direction and b refers to the wing root chord length. The deformation of the wing surface has the largest vertical displacement of approximately 7% with respect to the wing root chord length. It can be seen from Figure 4 that the static aeroelastic equilibrium has been achieved with the convergence of the residuals.

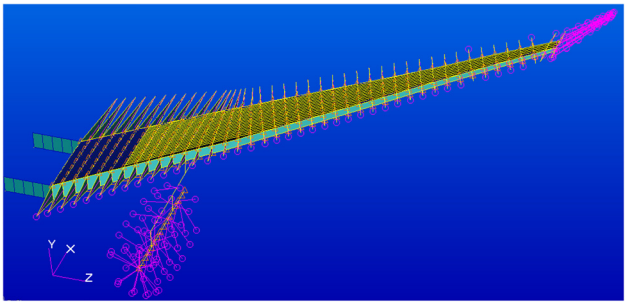

Figure 2: Structure finite element model.

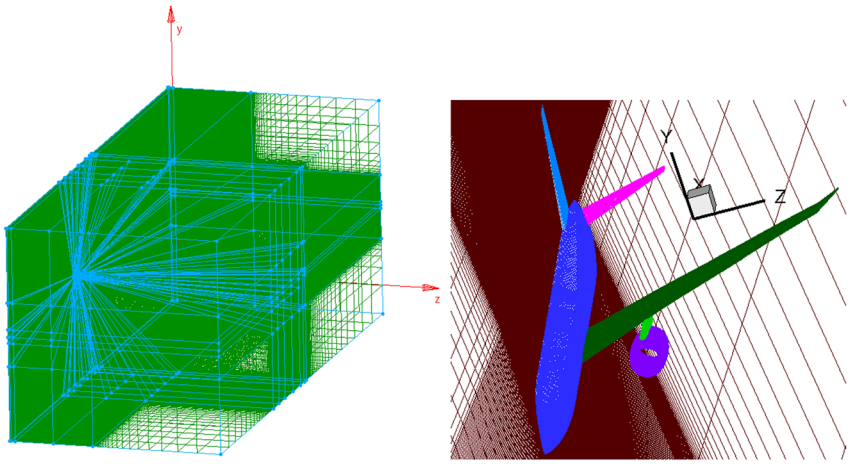

Figure 3: (a) Fluid field mesh and (b) surface mesh and symmetry plane mesh.

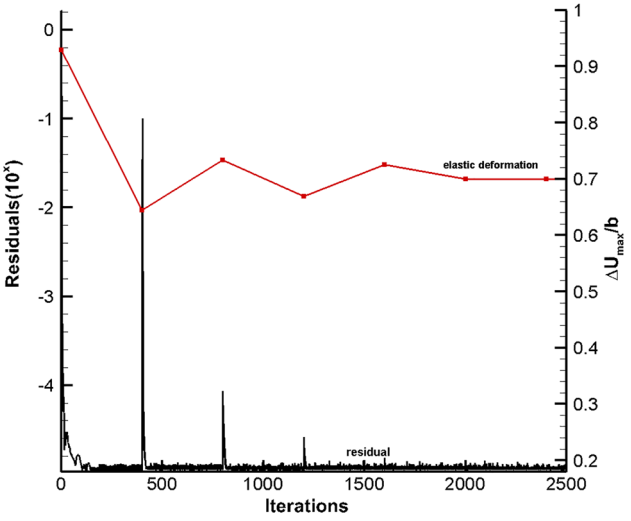

Figure 4: The convergence of residuals and the maximum displacement on surface.

Figure 5 shows the comparison of the pressure distribution for the body surface at the angle of attack of 8° between the linear and nonlinear static analysis. It shows there is a significant horizontal displacement in nonlinear case as compared to the linear computation.

Figure 6 shows the comparison of the twist angles of the spanwise section between the linear and nonlinear analysis at the angle of attack 8°. From this figure, it can be seen that the large negative twist angle is observed for the linear case as compared to the nonlinear computation.

Figure 7 shows the linear and nonlinear spanwise deflection at different angles of attack, respectively. It can be seen from the two figures that the horizontal deflection in nonlinear computation is larger than that in linear case with the increment of the angle of attack, while the vertical deflection is almost the same in the same flight condition. The significant changes in the horizontal displacement arise from the increase of torsion component. The results seem different from the study by Mian [15] which pointed that for the linear case there is no axial deflection in the structure. The reason is that they studied the geometrical nonlinear effect with the beam to replace the real structure, and in the linear computation the displacement in the horizontal direction is neglected for the beam. In this article, the structure is modeled with the actual physical structure.

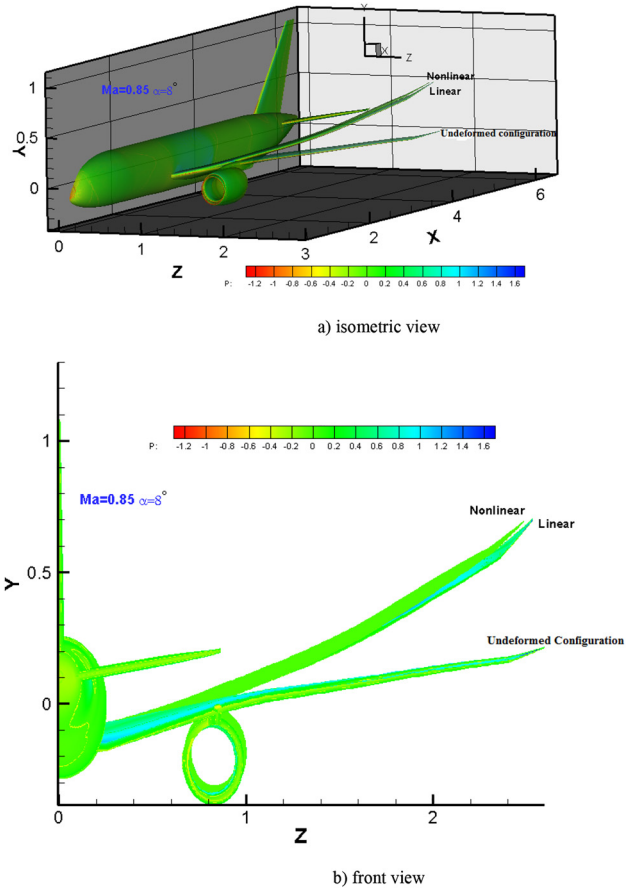

a) isometric view

b) front view

Figure 5: Pressure coefficient plot for linear and nonlinear cases.

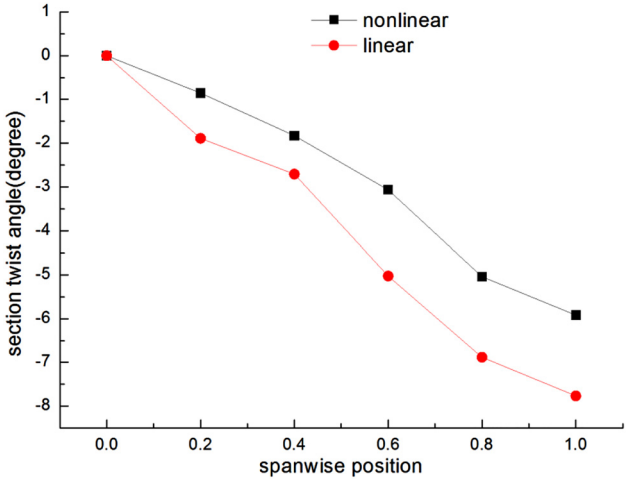

Figure 6: Spanwise section twist angle at Mach = 0.85 angles of attack of 8°.

The lift coefficients for linear and nonlinear cases comparison with the undeformed wing are shown in Figure 8. It can be seen that the lift coefficient of the linear structure is smaller than the nonlinear case, which is caused by the larger negative section twist angles of the linear computation described in Figure 6.

In order to compare the geometric nonlinear behavior and linear one, further computations were performed. While bending moment and torque are the overriding aerodynamic moments suffered by airplanes in flight, they are calculated in center of rigidity of the different profiles along the spanwise (the origin of the coordinates located in the nose) and shown in Figure 9 to highlight the difference between the linear and the

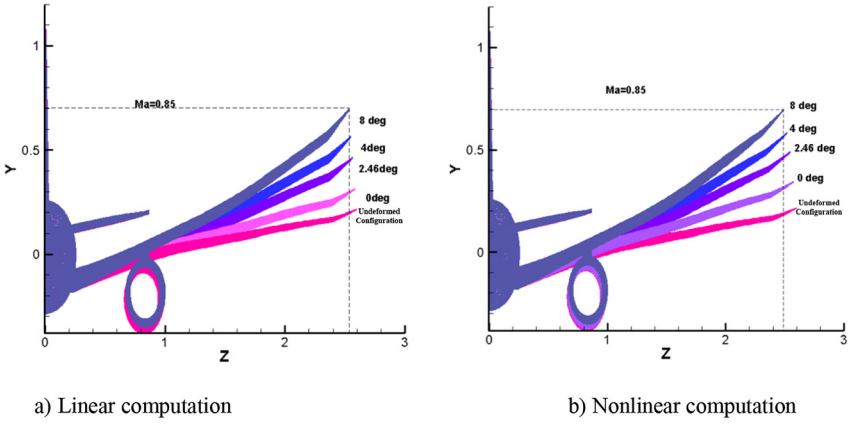

a) Linear computation b) Nonlinear computation

Figure 7: Spanwise displacement for different attack angles at Mach = 0.85.

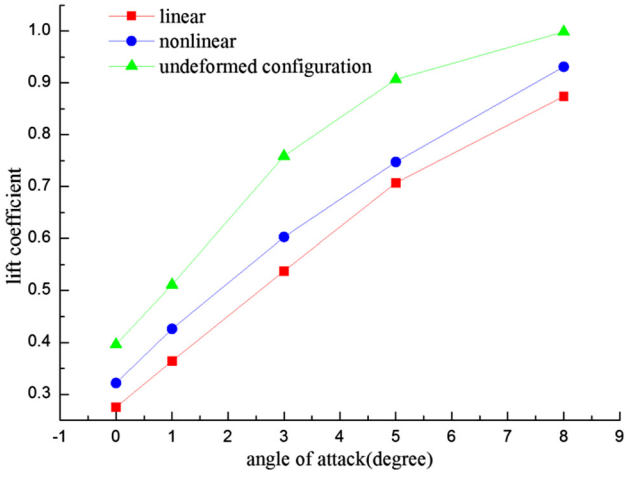

Figure 8: Lift coefficients for different attack angles at Mach = 0.85.

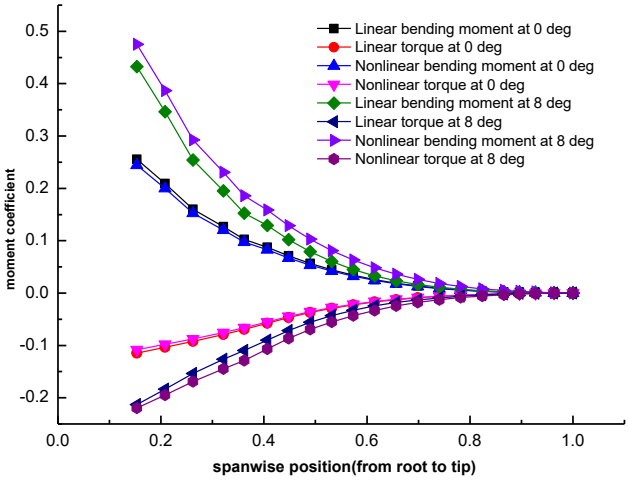

Figure 9: Bending moment and torque at Mach = 0.85 along the spanwise.

nonlinear analysis in different angles of attack. The moment coefficients at the angle of attack of 0° show only very small differences between the linear and nonlinear structure, which are expected since the structural deflections at this attack angle are nearly identical. In this condition, the linear structure model has the ability to calculate structure deformation. The discrepancy of moment coefficients becomes more significant at the attack angle of 8°, at which visible differences of structural deflections occur between the two structures. This means that the nonlinear analysis must be used to get more accurate results due to geometrical nonlinearity.

4 Conclusion

Nonlinear static aeroelasticity numerical simulation of the high-aspect-ratio wing has been conducted. To consider geometrical nonlinearity of such a wing, the in-house CFD/CSD coupling solver is introduced. The geometrically nonlinear and linear behaviors have been compared and evaluated. The results show that the CFD/CSD coupling method developed in this study can be used to accurately provide information about the 3-D solution.

The numerical results presented for the static aeroelastic analysis show that at the same Mach number, the linear and nonlinear effects are slightly different at the small angle of attack where the flow condition cannot sufficiently generate the geometric structural nonlinearity. However, with the increment of the angles of attack, the small deformation assumption cannot account for the geometrical nonlinearity. The change in stiffness of the structure must be considered when the structure suffers from large deformation. The calculated results indicate that the geometrically nonlinear displacement is greater than the linear one along the spanwise, wherever they have a slight difference along the vertical, which arise from the more torsion components coupled due to geometrical nonlinearity. It can also draw a conclusion that for practical applications, the solution based on the linear elasticity theory gives fairly accurate results in predicting deformations and stress resultants for reasonable attack angles.

Future work will focus on the impact of the geometrical nonlinearity on the flutter speeds of large aspect ratio wing.

Acknowledgements: This work is supported by the National Natural Science Foundation (No. 11672303 and No. 11702298).
Author contribution: All the authors have accepted responsibility for the entire content of this submitted manuscript and approved submission.
Research funding: None declared.
Conflict of interest statement: The authors declare no conflicts of interest regarding this article.

References

[1] M. J. Patil and D. H. Hodges, "Limit cycle oscillations in high-aspect-ratio Wings," in *AIAA-99-1464*, 1999.
[2] M. J. Patil and D. H. Hodges, "On the importance of aerodynamic and structural nonlinearities in aeroelastic behavior of high -aspect-ratio wings," in *AIAA 2000-1448*, 2000.
[3] M. J. Smith, M. J. Patil, and D. H. Hodges, "CFD-based analysis of nonlinear aeroelastic behavior of high-aspect ratio wing," in *AIAA 2001-1582*, Williamsburg, USA, 1999.
[4] D. Petot, "Differential equation modeling of dynamic stall," *Recherche aerospatiale Technical translation*, vol. 5, pp. 59–72, 1989.
[5] J. A. Garcia and G. P. Guruswamy, "Aeroelastic analysis of transonic wings using Navier-Stokes equations and a nonlinear beam finite element model," in *AIAA-1999-1215*, 1999.
[6] R. Palacios and C. E. S. Cesnik, "Static nonlinear aeroelasticity of flexible slender wings in compressible flow," in *AIAA 2005 1945*, 2005.
[7] J. Blazek, *Computational Fluid Dynamics: Principles and Applications*, Oxford, Elsevier, 2001.
[8] P. L. Roe, "Approximate Riemann solvers, parameter vectors, and difference schemes," *J. Comput. Phys.*, vol. 43, pp. 357–372, 1981.
[9] G. W. Yang, G. N. Zheng, and G. B. Li, "Computational methods and engineering applications of static/dynamic aeroelasticity based on CFD/CSD coupling solution," *Sci. China Technol. Sci.*, vol. 55, no. 9, pp. 2453–2461, 2012.
[10] MSC.Software Corporation, *MSC Nastran 2011 Implicit Nonlinear (SOL 600) User's Guide*, 2011.
[11] K. L. Bathe, E. Ramm, and E. L. Wilson, "Finite element formulations for large deformation dynamic analysis," *Int. J. Numer. Methods Eng.*, vol. 9, pp. 353–386, 1975.
[12] A. K. Michler, "Aircraft control surface deflection using RBF-based mesh deformation," *Int. J. Numer. Methods Eng.*, vol. 88, pp. 996–1007, 2011.
[13] A. Beckert and H. Wendland, "Multivariate interpolation for fluid–structure interaction problems using radial basis functions," *Aero. Sci. Technol.*, vol. 5, pp. 125–134, 2001.

[14] T. C. S. Rendall and C. B. Allen, "Reduced surface point selection options for efficient mesh deformation using radial basis functions," *J. Comput. Phys.*, vol. 229, no. 8, pp. 2810–2820, 2010.
[15] H. H. Mian, G. Wang, and Z. Y. Ye, "Numerical investigation of structural geometrical nonlinearity effect in high-aspect-ratio wing using CFD/CSD coupled approach," *J. Fluid Struct.*, vol. 49, pp. 186–201, 2014.